The Confinement of Mortar in Masonry Under Compression: Experimental Data and Micro-Mechanical Analysis

Anastasios Drougkas , Els Verstrynge , Roald Hayen , Koenraad Van Balen

PII: S0020-7683(18)30495-5
DOI: https://doi.org/10.1016/j.ijsolstr.2018.12.006
Reference: SAS 10205

To appear in: *International Journal of Solids and Structures*

Received date: 30 August 2018
Revised date: 5 November 2018

Please cite this article as: Anastasios Drougkas , Els Verstrynge , Roald Hayen , Koenraad Van Balen , The Confinement of Mortar in Masonry Under Compression: Experimental Data and Micro-Mechanical Analysis, *International Journal of Solids and Structures* (2018), doi: https://doi.org/10.1016/j.ijsolstr.2018.12.006

Highlights

- Experimental data on varied combinations of units and mortars are presented in detail
- The varying Poisson's ratio of mortar under compressive loading is investigated and modeled
- Computationally inexpensive and accurate micro-mechanical models are developed for the numerical reproduction of the experiments
- The influence of the material properties of mortar on the compressive behavior of masonry is highlighted
- The wide changes in the apparent vs. prescribed elastic properties of the material components in the masonry composite are shown

The Confinement of Mortar in Masonry Under Compression: Experimental Data and Micro-Mechanical Analysis

Anastasios Drougkas[1]

Building Materials and Building Technology Division, Civil Engineering Department, KU Leuven, Kasteelpark Arenberg 40 Box 2448, B-3001 Heverlee, Belgium

Els Verstrynge

Building Materials and Building Technology Division, Civil Engineering Department, KU Leuven, Kasteelpark Arenberg 40 Box 2448, B-3001 Heverlee, Belgium

Roald Hayen

Royal Institute for Cultural Heritage, Parc du Cinquantenaire 1, B-1000 Brussels, Belgium

Koenraad Van Balen

Building Materials and Building Technology Division, Civil Engineering Department, KU Leuven, Kasteelpark Arenberg 40 Box 2448, B-3001 Heverlee, Belgium

Abstract

The present paper deals with the behavior of several types of mortar in masonry under compression. The quantification of the response of mortar to triaxial confinement afforded by the masonry units in the composite subjected to compressive stresses is paramount in the determination of the peak stress of wallettes and pillars under compression. This behavior is greatly affected by the

[1] Corresponding author, email: anastasios.drougkas@kuleuven.be

behavior of the mortar micro-structure and is manifested by the constrained lateral expansion of the mortar in the joint.

A series of experimental results is presented, carried out on different assemblages of masonry composites (couplets and wallettes) with different types of masonry units and mortar, ranging in type from pure lime to cement based mortars. These experiments are subsequently simulated numerically using micro-mechanical techniques accounting for the shifting behavior of the Poisson's ratio of the mortar for varying levels of applied compression. Masonry is treated in a micro-mechanical framework as a composite material composed of two macroscopically distinct material phases: units and mortar.

The experiments and their simulation provide insight into the complexities of masonry under compression that need to be accounted for in numerical analysis, including a discussion on the progression of damage in each material phase. The results and their analysis are further enriched through a comparative parametric study. A clear difference emerges between the assigned and the apparent Poisson's ratio for the material components.

1. Introduction

1.1 State of the Art

The majority of existing and historic masonry structures is composed by regularly or semi-regularly arranged clay or stone units, bound through the use of mortar. The complexity of the structural behavior of masonry arises from the dimension ratios of the members, the brittle behavior of its constituent materials in tension and shear, and the geometrical complexity of the bond patterns. This complexity is further compounded by the mismatch of the elastic properties of the constituent materials, which leads to irregularities in the stress state at the meso-scale, particularly in the case of vertical, horizontal and diagonal compression.

Sophisticated numerical approaches are often required for the detailed analysis of masonry structures. Analysis methods for masonry in the macro-scale are able to capture the behavior of the material at the composite level [1], but are often reliant on the characterization of entire masonry samples [2], which present severe difficulties in their extraction and destructive testing. Micro-modeling approaches, on the other hand, rely on the distinct modeling of the material phases of the composite in order to achieve result completeness and a direct simulation of the interaction of the units and the mortar [3,4]. This is of particular importance for the study of masonry in compression and the three-dimensional interaction effects involved in the phenomenon [5,6].

An attractive method for the study of masonry composites is the micro-mechanical approach based on analytical expressions [7–10]. This allows for a relatively simple, versatile and computationally inexpensive method, compared to nonlinear finite element analysis, for micro-modeling of masonry composites without loss of accuracy.

The behavior of masonry in compression is greatly influenced by the mechanical characteristics of the mortar in the joints, which may exhibit different behavior in stand-alone samples and in the composite [11]. This is not limited to the uniaxial compressive or tensile strength of the material, but is a function, to a substantial degree, of its triaxial behavior as mobilized in the joint under confinement [12,13]. Due to their low Young's modulus, lime mortars are under higher levels of confinement compared to mortars with cement content [14]. This effect is enhanced in a computational context by the assumed high Poisson's ratio of these mortars, which results in greater calculated lateral expansion and subsequent restraint by the units. However, the Poisson's ratio is not constant but develops from an initially low value, owed to the high porosity of the material, to a very high value near the uniaxial strength limit, and is further influenced by its triaxial stress state [15]. Masonry mortars with high porosity are characterized by low uniaxial compressive strength and low initial Poisson's ratio.

Masonry composites composed of clay bricks and such mortars are characterized by a compressive strength several times the compressive strength of the mortar, which implies a significant amount of confinement in the joint which mobilizes the strength of the mortar under multiaxial confinement. A low Poisson's ratio would preclude the amount of confinement necessary for this high strength to develop. Therefore, the study of the stress state in the joint under perpendicular compression is of significant importance.

1.2 Objectives

In this paper a series of experimental tests on the compression of masonry triplets and Flemish bond wallettes are numerically simulated. The simulation is carried out using micro-mechanical models for masonry: a model for the analysis of Flemish bond wallettes and a newly developed model for stack bond masonry prisms. Different types of unit and mortar are studied, corresponding to a wide variety of combinations found in existing and historic structures, as well as in masonry composites used for reconstruction interventions.

Through the numerical simulations, it is sought to gain insight into the confinement effect afforded on the mortar joints by the units in masonry subjected to compression. This is achieved through the implementation of expressions for the development of the Poisson's ratio of mortar under varying levels of vertical stress and the quantification of the confinement of the mortar joint according to material and geometric parameters. The quantification allows for the adoption of a knowledge-based approach towards the prediction of the compressive strength of masonry based on the study of its constituent materials. In particular, the suitability of an approach based on a constant Poisson's ratio as an elastic parameter for the mortar is investigated and discussed.

The micro-mechanical approach adopted in this paper allows for a simple but inclusive overview of the development of damage in individual components (material phases) of the masonry composite

for an increasing load up to peak stress and beyond. Drawing from a wide spectrum of experimental data, and through parametric analyses, the influence of material and geometric parameters are evaluated and valorized.

2. Experimental Data

2.1 Tests on Clay Units

The units are hand-molded solid clay bricks measuring $188 \times 48 \times 88 mm^3$. Cubic samples, produced by cutting with a diamond saw, with dimensions $40 \times 40 \times 40 mm^3$ were tested in uniaxial compression. Longitudinal deformation was measured using four perimetrically arranged linear variable differential transformers (LVDTs) attached to the load plates. Lateral expansion was measured using four horizontal LVDTs. Prismatic samples with dimensions $160 \times 40 \times 40 mm^3$ were tested in three-point bending. Two batches of the same type of units were tested, both of which, produced similar results. The average results of the two batches of the material characterization are presented in Table 1. Of note is the particularly high scatter for the Poisson's ratio, while the compressive strength, Young's modulus and flexural strength exhibited lower, but still substantial, scatter.

Due to the lack of generally accepted values for masonry components, missing material properties are calculated based on expressions used in concrete. The tensile strength was derived from the flexural strength according to the equation [16]:

$$f_t = f_f \frac{0.06h^{0.7}}{1 + 0.06h^{0.7}} \quad (1)$$

where h is the height of the specimen tested in three-point bending. The compressive fracture energy is calculated according to the equation [5]:

$$G_f^c = f_c d \tag{2}$$

where $d = 1mm$. The tensile fracture energy in N/mm is calculated according to the equation [16]:

$$G_f^t = \frac{73 f_c^{\,0.18}}{1000} \tag{3}$$

with the compressive strength f_c in N/mm^2.

Table 1 Material properties of clay bricks (coefficient of variation in parentheses).

Young's modulus	E	$[N/mm^2]$	2570 (0.297)
Poisson's ratio	ν	$[-]$	0.14 (0.500)
Compressive strength	f_c	$[N/mm^2]$	9.97 (0.225)
Flexural strength	f_f	$[N/mm^2]$	3.12 (0.151)
Tensile strength	f_t	$[N/mm^2]$	1.37
Compressive fracture energy	G_f^c	$[N/mm]$	9.97
Tensile fracture energy	G_f^t	$[N/mm]$	0.110

2.2 Tests on Mortars

Two batches of mortar were produced, tested and employed in the construction of the masonry samples. The mortars include a) a lime putty mortar (LP), b) a natural hydraulic lime mortar (HL), c) a hybrid lime-cement mortar (LC) and d) a cement mortar (CM). Batch A mortars were used for the construction of the masonry triplets, while batch B mortars were used in the Flemish bond wallettes and for the determination of the triaxial behavior characteristics of the mortar. The two mortar batches were produced at different time periods, with variations of the binder and aggregate content in order to maximize material variety. The compositions of the mortars are given in Table 2. Batch B LC mortars were made using a commercial premix (Unilit 35). The weight percentages of binder and aggregates are presented jointly in this case under the sand column.

Table 2 Overview of mortar compositions in weight percentage.

		Binder	Sand	Water
Batch A	LP	14.1	65.9	20.0
	HL	11.2	71.2	17.6
	LC	5.8 L + 8.9 C	68.8	16.8
	CM	17.6	67.8	14.6
Batch B	LP	22.3	71.2	5.8
	HL	-	87.5 (premix)	12.5
	LC	10.9 L + 6.3 C	73.0	9.8
	CM	18.2	70.0	11.8

Compressive and three-point bending tests on the mortars were carried out according to the EN testing standard [17]. The results are summarized in Table 3 and Table 4 for the results at the age of testing of the masonry samples. The adjustment of the Young's modulus and Poisson's ratio of the batch B mortars was carried out in order for the model of the masonry to approach the experimentally derived stiffness of the wallettes in compression. The range indicated in the Poisson's ratio of the mortar defines the initial and maximum values of the material parameter as implemented in the micro-mechanical modeling of the mortar in compression. The difference between the value assigned as a material parameter, be it a constant value or determined through a constitutive relation with applied stress, and the apparent value, as determined through the deformation of the material, is discussed in section 6.

Table 3 Material properties of batch A mortars (coefficient of variation in parentheses).

			Lime putty mortar	Hydraulic lime mortar	Lime-cement mortar	Cement mortar
Young's modulus	E	$[N/mm^2]$	96 (0.375)	762 (0.434)	235 (0.434)	3325 (0.494)
Poisson's ratio	ν	$[-]$	0.05-0.25	0.05-0.25	0.05-0.25	0.05-0.25
Compressive strength	f_c	$[N/mm^2]$	0.79 (0.114)	4.47 (0.063)	1.68 (0.167)	19.47 (0.063)
Flexural strength	f_f	$[N/mm^2]$	0.52 (0.058)	1.34 (0.082)	0.79 (0.063)	3.67 (0.076)
Tensile strength	f_t	$[N/mm^2]$	0.23	0.59	0.35	2.57
Compressive fracture energy	G_f^c	$[N/mm]$	0.79	4.47	1.68	19.47
Tensile fracture energy	G_f^t	$[N/mm]$	0.070	0.096	0.080	0.125

Table 4 Material properties of batch B mortars (coefficient of variation in parentheses).

			Lime putty mortar	Hydraulic lime mortar	Lime-cement mortar	Cement mortar
Young's modulus	E	$[N/mm^2]$	200	400	1000	10000
Poisson's ratio	ν	$[-]$	0.05-0.30	0.05-0.25	0.05-0.30	0.05-0.25
Compressive strength	f_c	$[N/mm^2]$	1.45 (0.062)	0.89 (0.124)	1.7 (0.035)	14.4 (0.085)
Flexural strength	f_f	$[N/mm^2]$	0.45 (0.089)	-	0.79 (0.063)	5.81 (0.060)
Tensile strength	f_t	$[N/mm^2]$	0.20	0.12	0.35	2.57
Compressive fracture energy	G_f^c	$[N/mm]$	1.45	0.89	1.7	14.4
Tensile fracture energy	G_f^t	$[N/mm]$	0.078	0.071	0.080	0.118

2.3 Tests on Masonry Samples

The triplets consisted in simply stacked units with masonry bed joints. The dimensions of the samples were $188 \times 164 \times 88\,mm^3$ (length × height × width). They were tested in an INSTRON 1196 machine, with a capacity of $250\,kN$. The Flemish bond wallettes were three units in length and 10 courses high. The samples measured $584 \times 570 \times 186\,mm^3$. They were tested in an INSTRON 8800 machine with a capacity of $2500\,kN$. All masonry samples were tested under displacement-controlled loading. A constant strain rate was maintained, equal to $0.1\,mm/min$. A gypsum compensating layer was introduced between the load surface on the samples and the load plates. The in-plane deformation of the samples was measured using horizontally and vertically arranged LVDTs.

The results of the masonry triplets and Flemish bond wallettes are presented in Table 5 and Table 6 respectively indicating the obtained compressive strength and the macroscopic Young's modulus. Generally, the Flemish bond wallettes exhibited a higher stiffness than the triplets, but also a lower compressive strength, as in the case of the LC mortar in particular. Differences in the compressive strength are expected between triplets and wallettes due to the differences in dimensions, which in turn can also affect mortar confinement, and the geometric bond of the units, which introduces a greater number of planes of weakness in the composite.

Table 5 Properties of masonry triplets (coefficient of variation in parentheses).

			Lime putty mortar	Hydraulic lime mortar	Lime-cement mortar	Cement mortar
Young's modulus	E	$[N/mm^2]$	296 (0.152)	670 (0.343)	985 (0.207)	865 (0.138)
Compressive strength	f_c	$[N/mm^2]$	4.54 (0.207)	5.94 (0.136)	8.12 (0.105)	9.00 (0.020)

Table 6 Properties of masonry Flemish bond wallettes (coefficient of variation in parentheses).

			Lime putty mortar	Hydraulic lime mortar	Lime-cement mortar	Cement mortar
Young's modulus	E	$[N/mm^2]$	636 (0.149)	1374 (0.184)	2734 (0.149)	3729 (0.114)
Compressive strength	f_c	$[N/mm^2]$	4.19 (0.002)	5.93 (0.105)	4.70 (0.343)	8.36 (0.030)

3. Micro-Mechanical Model

3.1 Overview

The method of cells constitutes a wide-spread approach in the field of the analysis of composite materials characterized by a repeating geometric pattern [18]. The composite is discretized into repeating unit cells, each geometrically representative of the entire composite. These cells are further discretized into sub-cells according to the geometrical arrangement of the two or more material phases comprising it. The sub-cells are finally assigned different material properties and their interaction is accounted for.

In the present study, the interaction of the sub-cells, here called cuboids, is modeled using closed form expressions, derived from stress equilibrium and deformation conformity within the cell. The main advantage of using closed form expressions is the marked reduction in the computational cost. Additional rational assumptions are made concerning the distribution of stresses between the cuboids. An analytical model for the calculation of the stresses and strains in a layered masonry pillar, comprised of alternating layers of units and mortar, was proposed by Haller [7]. In this model the horizontal and transversal strains are equal in both layers, therefore the length and the width of the masonry unit are not parameters in the calculation, and there is no distinction between horizontal and

transversal stress and strain. In the present work a refinement of this model is proposed which introduces these geometrical parameters and results in different stresses and strains in the two directions orthogonal to the loading direction.

The common assumptions for all models are summarized here. Each cuboid n is characterized by constant stress and strain in three orthogonal directions, arbitrarily denoted as i, j and k. According to Hooke's law, the normal and shear stresses and strains are related according to the following equation:

$$\varepsilon_{ii,n} = \sigma_{ii,n}/E_n - \nu_n\left(\sigma_{jj,n} - \sigma_{kk,n}\right)/E_n \tag{4}$$

$$\varepsilon_{ij,n} = \sigma_{ij,n}\left(1 + \nu_n\right)/E_n \tag{5}$$

where σ and ε are the stresses and strains respectively, E is the Young's modulus, ν is the Poisson's ratio. The deformation of the cuboid due to normal and shear strain is assumed equal to:

$$d_{i,n} = \varepsilon_{ii,n}D_{i,n} + \varepsilon_{ij,n}\frac{D_{j,n}}{2} + \varepsilon_{ik,n}\frac{D_{k,n}}{2} \tag{6}$$

where $D_{i,n}$, $D_{j,n}$ and $D_{k,n}$ is the length of the cuboid in direction i, j and k respectively.

Normal and shear stress equilibriums at the faces of the cells with dimensions D_i, D_j and D_k are as follows:

$$\sum_m \sigma_{ii,m}D_{j,m}D_{k,m} - \sigma_{ii}D_jD_k = 0 \tag{7}$$

$$\sum_m \sigma_{ij,m}D_{i,m}D_{k,m} - \sigma_{ij}D_iD_k = 0 \tag{8}$$

$$\sum_m \sigma_{ij,m}D_{j,m}D_{k,m} - \sigma_{ij}D_jD_k = 0 \tag{9}$$

where σ_{ii} and σ_{ij} are the externally applied normal and shear stresses on the cell and m indicates a cuboid at the edge of the cell.

3.2 Unit cells: derivation and discretization

For all calculations suffix x denotes the longitudinal, y the vertical and z the transversal direction with respect to the layout of the masonry. Normal stress and strain components are denoted with a double suffix of the same symbol, and two different symbols denote a shear component. The type of cuboid is itself designated in a suffix: u and m signify the units and mortar in the stack bond pillar model, while for the Flemish bond model, s and d signify stretcher and header units respectively, and h, c, b and t signify head, cross, bed and transversal, or collar, joints respectively. Additional number suffixes are used where several unit or mortar cuboids of the same type are found in the model. For the dimensions of the cuboids, l signifies the longitudinal direction, h the vertical and t the transversal dimension. The derivation of the unit cells from stack bond pillars and Flemish bond walls is shown in Figure 1. The discretization of the periodic unit cells, along with the nomenclature of the resulting cuboids and the assigned dimensions, is illustrated in Figure 2.

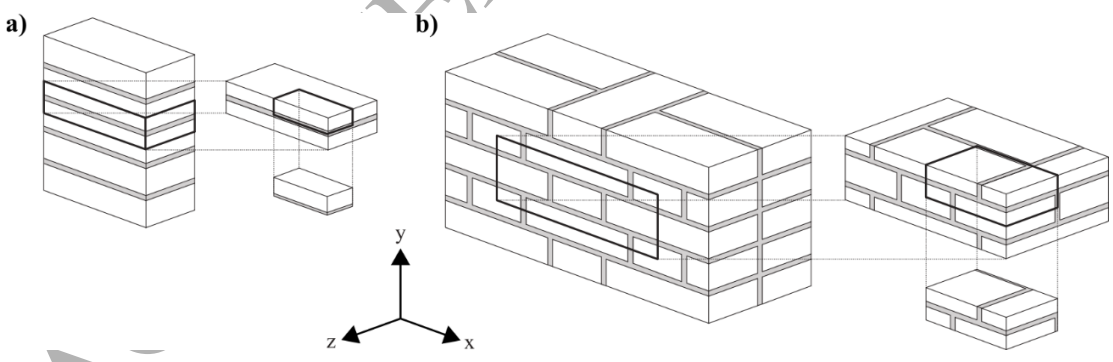

Figure 1 Derivation of periodic unit cells: a) stack bond pillar and b) Flemish bond wall.

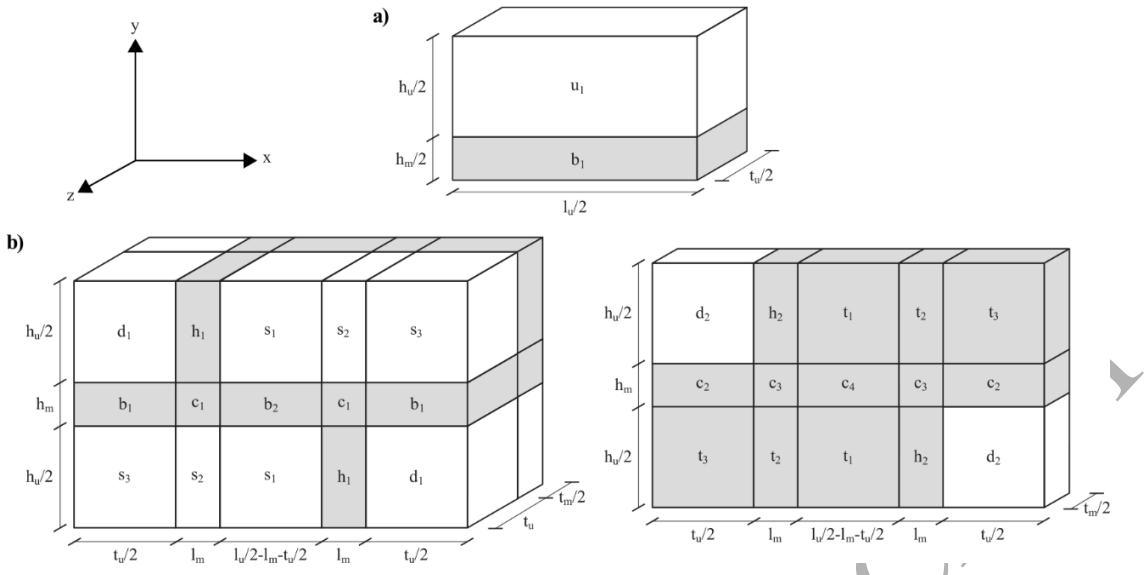

Figure 2 Discretization of periodic unit cells into cuboids: (a) stack bond pillar and (b) Flemish bond wall (external and middle leaf).

3.3 Models for stack bond pillars and Flemish bond walls

The stress and strain conformity equations and the calculation of the total strains in the Flemish bond cell, all related to linear elastic analysis, are presented in detail in [9] and are not repeated here for the sake of brevity. The implemented changes in nonlinear analysis as against [19] are detailed in the following section.

In Haller's original model for stack bond masonry prisms, strains lateral to the loading direction are considered equal in the two material phases. Further, the stresses and strains in the horizontal and transversal directions are equal, therefore no real distinction arises in these directions and the length and width of the unit are not considered in the calculations: the height of the unit and the mortar joint are the only geometrical parameters in the equations.

A modification of this model is proposed here. The modification in the stack bond prism model consists in differentiating between the two lateral directions and including the dimensions of the unit, while additionally producing a lower amount of confinement on the mortar joint.

Due to horizontal and transversal stress equilibrium, the resulting conformity equations are:

$$\sigma_{xx}(h_m + h_u) = \sigma_{xx,u}h_u + \sigma_{xx,b}h_m \tag{10}$$

$$\sigma_{zz}(h_m + h_u) = \sigma_{zz,u}h_u + \sigma_{zz,b}h_m \tag{11}$$

Vertical stress equilibrium, given that the vertical stress is equal in both components, reads:

$$\sigma_{yy,u} = \sigma_{yy,m} = \sigma_{yy} \tag{12}$$

Strain equality is enforced between the unit and the mortar joint in the longitudinal direction:

$$\varepsilon_{xx,u} = \varepsilon_{xx,m} \tag{13}$$

Finally. the ratio of longitudinal to transversal stress in the unit is assumed to be equal to the ratio of length over width of the unit in order to proportion the difference in confinement in the two directions according to the geometric layout:

$$\sigma_{xx,u}t_u = \sigma_{zz,u}l_u \tag{14}$$

According to the above approach, the ratio of horizontal or transversal stress in the mortar joint over the applied vertical stress is determined to be equal to:

$$\frac{\sigma_{xx,m}}{\sigma_{yy}} = \frac{h_u l_u (E_m v_u - E_u v_m)}{E_m h_m (t_u v_u - l_u) + E_u h_u (t_u v_m - l_u)} = s_{m,x} \tag{15}$$

$$\frac{\sigma_{zz,m}}{\sigma_{yy}} = \frac{h_u(E_m l_u v_u - E_u t_u v_m)}{E_m h_m(t_u v_u - l_u) + E_u h_u(t_u v_m - l_u)} = s_{m,z} \tag{16}$$

For Haller's model the $s_{m,x}$ and $s_{m,z}$ parameters are equal and calculated according to the equation

$$s_m = \frac{E_m h_u v_u - E_u h_u v_m}{E_m h_m v_u + E_u(h_u v_m - h_u) - E_m h_m} \tag{17}$$

The Young's modulus of the masonry composite E_c, assuming constant values for all elastic parameters, may also be derived from the above equations, and is equal to:

$$E_c = \frac{E_m E_u(h_u + h_m)\left(E_m h_m(t_u v_u - l_u) + E_u h_u(t_u v_m - l_u)\right)}{\begin{array}{l} E_m h_m\left(E_m h_u\left((t_u + l_u){v_u}^2 - l_u\right) + \left(E_u(h_m t_u h_u - 2(t_u + l_u)v_m) + E_m h_u t_u\right)v_u\right) + \\ E_u\left(E_u h_m h_u\left(v_m\left((t_u + l_u)v_m + t_u\right) - l_u\right) + E_m\left({h_u}^2 t_u v_m - l_u\left({h_u}^2 + {h_m}^2\right)\right)\right) \end{array}} \tag{18}$$

For Haller's model the expression for the Young's modulus of masonry is

$$E_c = \frac{E_m E_u(h_u + h_m)(E_m h_m v_u + E_u h_u(v_m - 1) - E_m h_m)}{\begin{array}{c} {E_m}^2 h_m h_u(2{v_u}^2 - 1) + \\ E_m h_m(E_u(h_m - 4h_u v_m) + E_m h_u)v_u + \\ {E_u}^2 h_m h_u(2{v_m}^2 + v_m - 1) + \\ E_u E_m\left({h_u}^2 v_m - \left({h_u}^2 + {h_m}^2\right)\right) \end{array}} \tag{19}$$

Disregarding the influence of the Poisson's ratio of the components, thus treating the layered composite as a linear series of springs with no longitudinal and transversal interaction, the above equation becomes:

$$E_{c,s} = \frac{E_m E_u(h_u + h_m)}{E_m h_u + E_u h_m} \tag{20}$$

Significant differences in the calculated Young's modulus of masonry may arise from the inclusion of the Poisson's ratio of the mortar in the calculation. Assuming a material combination of the above

described clay units and the lime putty mortar, the ratio of the Young's modulus of the masonry composite according to the proposed (eq. 18) or Haller (eq. 19) model and the simple spring model (eq. 20) is shown in Figure 3. The Young's modulus of the masonry composite increases significantly, particularly in the case of Haller's model, for higher values of the Poisson's ratio of the mortar, which may indeed be registered for high levels of applied stress. This effect, however, is in practice partially offset by the decrease in the tangent Young's modulus of the mortar due to crushing under high applied loads.

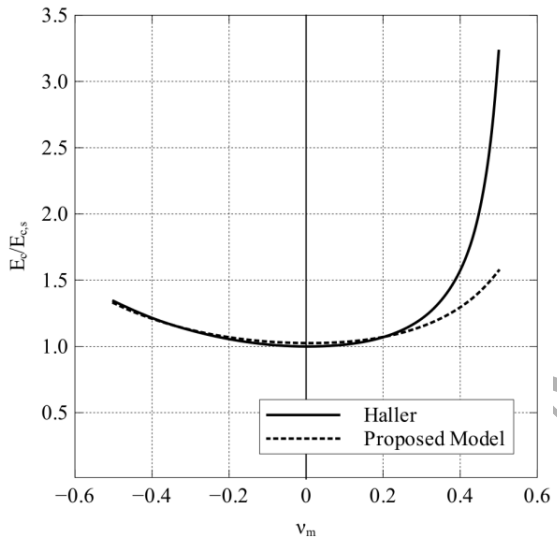

Figure 3 Comparison of Young's modulus of masonry according to Haller's model and the proposed model both denoted E_c, vs. the simple spring model $E_{c,s}$ for variation of the Poisson's ratio of mortar.

3.4 Nonlinear analysis

Nonlinear analysis of the periodic unit cell is performed by applying a normal strain in the cell, calculating the internal stresses in the cuboids and deriving an averaged stress at the faces of the cell. The constitutive modeling of the nonlinearity of the cuboids in compression and tension is achieved

through the adoption of integrity variables linking the effective stress, which is proportional to the strain, to the actual or "damaged" stress [19]. Integrity variables assume values between 1, indicating a completely undamaged material, to 0, indicating a completely damaged material.

The integrity variable for each cuboid n in compression at analysis step i is equal to:

$$C_n(i) = \begin{cases} 1 & if \quad 0 \le \varepsilon(i) \le \varepsilon_{c/3} \\ -\frac{f_c}{\sigma_{eff,n}(i)}\frac{1}{3}\left(1 + 4\frac{\varepsilon(i) - \varepsilon_{c/3}}{\varepsilon_c - \varepsilon_{c/3}} - 2\left(\frac{\varepsilon(i) - \varepsilon_{c/3}}{\varepsilon_c - \varepsilon_{c/3}}\right)^2\right) & if \quad \varepsilon_{c/3} \le \varepsilon(i) \le \varepsilon_c \\ -\frac{f_c}{\sigma_{eff,n}(i)}\left(1 - \left(\frac{\varepsilon(i) - \varepsilon_c}{\varepsilon_u - \varepsilon_c}\right)^2\right) & if \quad \varepsilon_c \le \varepsilon(i) \le \varepsilon_u \\ 0 & if \quad \varepsilon_u \le \varepsilon(i) \end{cases} \tag{21}$$

where f_c is the compressive strength, ε is the strain and $\sigma_{eff,n}$ is the effective stress in the direction being evaluated. Compressive stresses and strains assume negative values. The strain $\varepsilon_{c/3}$ is the limit of proportionality in compression, equal to $\varepsilon_{c/3} = -\frac{1}{3}\frac{f_c}{E}$ (22)

ε_c is the peak strain

$$\varepsilon_c = -\frac{5}{3}\frac{f_c}{E} \tag{23}$$

and ε_u is the ultimate strain

$$\varepsilon_u = \varepsilon_c - \frac{3}{2}\frac{G_f^c}{f_c h} \tag{24}$$

where G_f^c is the compressive fracture energy and h is the characteristic length, equal to the dimension of the cuboid in the evaluated direction of loading. The above expressions describe a parabolic actual stress/strain curve in compression based on fracture energy according to Feenstra [20].

The integrity variable in tension at analysis step i is equal to

$$T_n(i) = \begin{cases} 1 & if \quad 0 \le \varepsilon(i) \le \varepsilon_t \\ \dfrac{f_t}{\sigma_{eff,n}(i)} exp\left(-\dfrac{f_t h}{G_f^t} (\varepsilon(i) - \varepsilon_t) \right) & if \quad \varepsilon_t \le \varepsilon(i) \end{cases} \tag{25}$$

where f_t is the tensile strength and ε_t is the limit of proportionality in tension, equal to the peak strain

$$\varepsilon_t = \frac{f_t}{E} \tag{26}$$

and G_f^t is the tensile fracture energy. Tensile stresses and strains assume positive values. The characteristic length h is again equal to the dimension of the cuboid in the evaluated direction. The above equations describe an exponential softening curve in tension based on fracture energy according to Feenstra [20].

Through the evaluation of the integrity variables in three directions it is possible to directly incorporate the effects of anisotropy in terms of material strength in the model, as might be encountered in the units. Similarly, elastic anisotropy can easily be taken into account in a simple modification of the Hooke's law equations. This can be of use for the analysis of extruded and cut clay units, which can present orthotropic elastic behavior. This path has not been pursued in the present study, even though the analysis framework is fully functional in that regard.

The integrity variables in tension and compression are evaluated in the three principal directions of the cuboid, assuming that the stress is positive or negative respectively. An isotropic damage approach is adopted, and no damage recovery is allowed for unloading. The actual stress for each cuboid n at step i is finally equal to

$$\sigma_n(i) = C_n(i)T_n(i)\sigma_{eff,n}(i) \tag{27}$$

The interaction of lateral stress in the compressive strength of the units is taken into account through a Mohr-Coulomb type curve in the compression-tension range. When tensile stress σ_l is applied laterally in the direction where the compressive integrity variable is evaluated, the compressive strength of the unit is scaled down to $f_{c,l}$, which is assumed equal to

$$f_{c,l} = (1 - \sigma_l/f_t)f_c \tag{28}$$

The strain values in the parabolic curve are scaled down proportionally. No increase in the compressive strength of the units is considered due to biaxial or triaxial compression.

The increase in the compressive strength of the mortar due to biaxial or triaxial compression is taken into account through the Hsieh-Ting-Chen failure curve [21]. In terms of principal stresses σ_1, σ_2 and σ_3 the criterion is expressed as

$$f = A\frac{J_2}{f_c{}^2} + B\frac{\sqrt{J_2}}{f_c} + C\frac{\sigma_1}{f_c} + D\frac{I_1}{f_c} - 1 = 0 \tag{29}$$

where I_1 and J_2 are the first stress and second deviatoric stress invariants respectively, and σ_1 is the maximum principal stress. The numerical parameters A, B, C and D are calculated according to the results of uniaxial tension, uniaxial compression, biaxial compression and triaxial compression under equibiaxial stress. The confined compressive strength of the mortar is acquired by solving the equation for σ_3, with σ_1 and σ_2 being the actual lateral stresses applied in the cuboid ($\sigma_1 > \sigma_2$). The pre-peak part of the parabolic compression curve is scaled proportionally to the ratio of the confined compressive strength over the uniaxial compressive strength. In the initial calculations the values proposed for concrete in [21] will be used for determining the failure curve. These values are

calculated by a tensile strength equal to 10% of the uniaxial compressive strength, a biaxial strength equal to 1.15 times the uniaxial compressive strength and a strength of 4.2 times the uniaxial strength under an equibiaxial confinement equal to 0.8 times the uniaxial strength.

The fitting of the experimental data on the triaxial compression of the batch B LP, HL and LC mortars is shown in Figure 4. The triaxial tests were carried out for the determination of the compressive strength σ_1 under a varying level of biaxial compression of $\sigma_2 = \sigma_3$. The fitting was performed only in the range where the confinement is limited to 50% of the apparent compressive strength: $\sigma_2 = \sigma_3 \leq 0.5\,\sigma_1$. The fitting for the LP and HL mortars is satisfactory. The failure curve appears to underestimate the confinement effect for lateral pressure less than 2.5 N/mm^2 in the LC case. The resulting numerical parameters for the mortars, along with the standard values for concrete, are presented in Table 7. Due to lack of experimental data in the current case, the standard concrete values were used for the CM mortar. Nevertheless, the high compressive strength of the CM mortar renders its behavior under confinement secondary in importance.

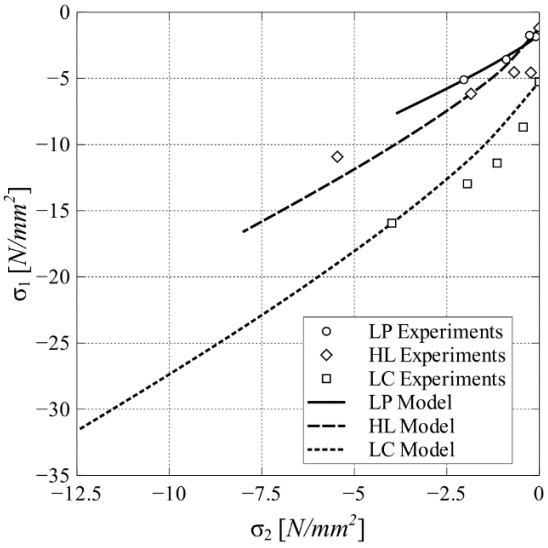

Figure 4 Fitting of experimental data on triaxial compression of mortars to Hsieh-Ting-Chen failure criterion.

Table 7 Numerical parameters for the Hsieh-Ting-Chen failure criterion: standard values for concrete and determined values for mortar.

Parameter	Concrete	LP	HL	LC
A	2.0108	7.378	4.3371	8.0331
B	0.9714	-1.6627	-0.1705	-1.9843
C	9.1412	10.2147	9.6066	10.3458
D	0.2312	0.4993	0.3473	0.5321

The constitutive relation of stress and strain, both in tension and in compression, is illustrated in Figure 5. Additionally, in the same figure the effect of confinement on the stress-strain curve in the compression range is indicated. As is shown, an increase in the compressive strength of the mortar due to confinement can result in increased brittleness, in terms of absolute difference between the peak and ultimate strain, since the compressive fracture energy is not increased. This behavior is consistent with abrupt failure observed in masonry samples with overly confined mortar joints [14].

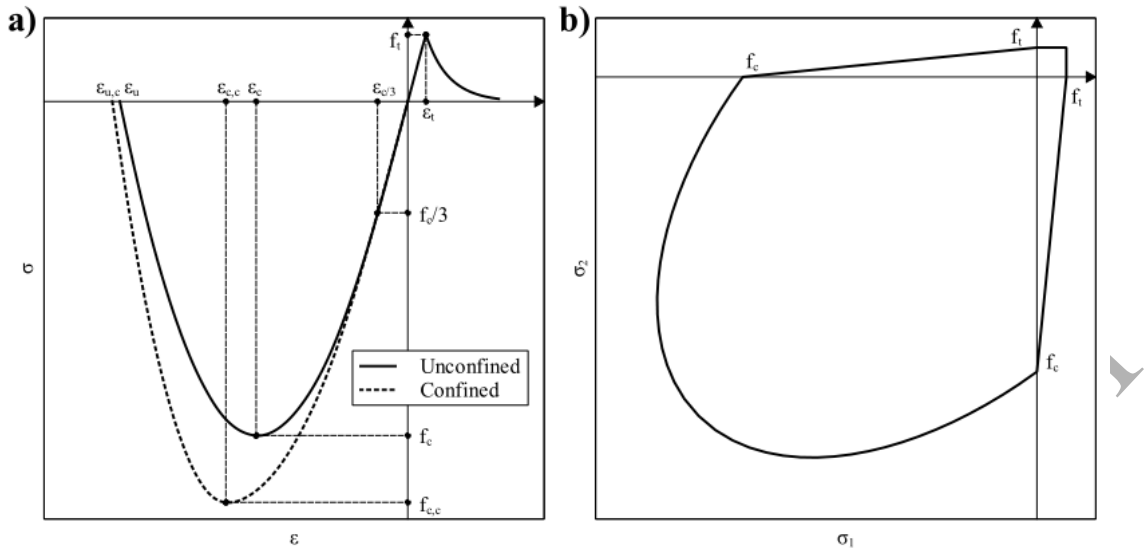

Figure 5 (a) Compression and tension stress-strain curves for unconfined and confined mortar. (b) Failure curve for mortar under biaxial stress.

3.5 The Poisson's ratio of mortar

The Poisson's ratio of mortar is here not considered constant as is usually the case in numerical analysis. Cementitious materials exhibit an increase in the Poisson's ratio for an increase in the applied compressive stress. This increase may in many cases be attributed to the porous structure of the mortar and its dilation due to crack formation [13]. The number of existing models for calculating the variation of the Poisson's ratio in cements and mortars under increasing compressive stress is limited. This variation may, as a first step, be modeled through use of the Ottosen model for concrete [22]. According to this model, the Poisson's ratio of mortar ν_m is equal to:

$$\nu_m(\beta) = \begin{cases} \nu_{m,1} & if \quad 0 < \beta \leq \beta_1 \\ \nu_{m,2} - (\nu_{m,2} - \nu_{m,1})\sqrt{1 - \dfrac{\beta - \beta_1}{1 - \beta_1}} & if \quad \beta_1 \leq \beta \leq 1 \\ \nu_{m,2} & if \quad 1 \leq \beta \end{cases} \tag{30}$$

where $\nu_{m,1}$ and $\nu_{m,2}$ are the initial and final Poisson's ratios respectively, β is the ratio of absolute actual compressive stress over the compressive strength and β_1 is the β ratio up to which the Poisson's ratio remains constant. It is assumed that the Poisson's ratio remains constant at its final value after attainment of the peak stress. The uniaxial compressive strength of the mortar is considered for the calculation of β regardless of an increase in the apparent compressive strength due to lateral confinement. The calculation of β and the Poisson's ratio therefore does not take into account the increase of the compressive strength due to confinement. Lateral confining stresses would retard the formation of cracks in the mortar and, therefore, affect the resulting Poison's ratio. Nevertheless, the adopted approach is a necessary simplification in light of the impracticality of carrying out experiments on mortar samples where the lateral pressure and the lateral displacement are simultaneously controlled while damage progress is monitored. This can be the object of future research using embedded sensors.

A further model linking the applied stress on the mortar and its Poisson's ratio has been proposed by Mohamad et al [15]. In this model the Poisson's ratio of the mortar is calculated as follows:

$$\nu_m(\beta) = \begin{cases} \nu_{m,1} e^{-\beta} & if \quad 0 < \beta \leq \beta_1 \\ \nu_{m,1} e^{\beta} & if \quad \beta_1 \leq \beta \end{cases} \tag{31}$$

The differences resulting from the two approaches for the Poisson's ratio are presented and discussed in the parametric investigation. The Ottosen and Mohamad models for the Poisson's ratio are graphically illustrated in Figure 6. Additionally, the confinement on the lime putty mortar joint, as quantified using the s_m, $s_{m,x}$ and $s_{m,z}$ parameters are also illustrated. The exponential increase of the ratio in the Mohamad model leads to an excessive amount of confinement. In a numerical framework, this can lead to instability. Furthermore, for a low initial value of the ratio, the Mohamad model can lead to a reversal in the confinement for low levels of stress: the unit is in triaxial compression and the

mortar is subjected to lateral tension. Therefore, the Ottosen model is applied here for the initial analyses.

A more general case of the Ottosen model is here proposed, which accounts for the Poisson's ratio for values of β higher than 1 but which does not result in an overestimation of the Poisson's ratio and, therefore, of the confinement of the mortar, as might happen in the Mohamad model for high values of compressive stress, since the value for $\nu_m(\beta)$ tends towards a prescribed value. Furthermore, the first inflection point is not restricted to a value of β equal to 1. The additional parameters of the proposed model allow for the fitting of experimental data of greater complexity, through the use of an initial, an intermediate and a final value of the Poisson's ratio. The model is expressed as:

$$\nu_m(\beta) = \begin{cases} \nu_{m,1} & if \quad 0 < \beta \leq \beta_1 \\ \nu_{m,2} - (\nu_{m,2} - \nu_{m,1})\sqrt{1 - \dfrac{\beta - \beta_1}{\beta_2 - \beta_1}} & if \quad \beta_1 \leq \beta \leq \beta_2 \\ \nu_{m,2} + (\nu_{m,3} - \nu_{m,2})\dfrac{\beta - \beta_2}{k + (\beta - \beta_2)} & if \quad \beta_2 \leq \beta \end{cases} \tag{32}$$

where β_2 is the β ratio for which the curve inflects for a second time and k is a numerical constant controlling the shape of the final hyperbolic curve of the model. For $\beta_1 = \beta_2 < 1$ and $\nu_{m,2} = \nu_{m,3}$ the model reverts to the Ottosen model. A comparison of the three models for the Poisson's ratio is shown in Figure 6.

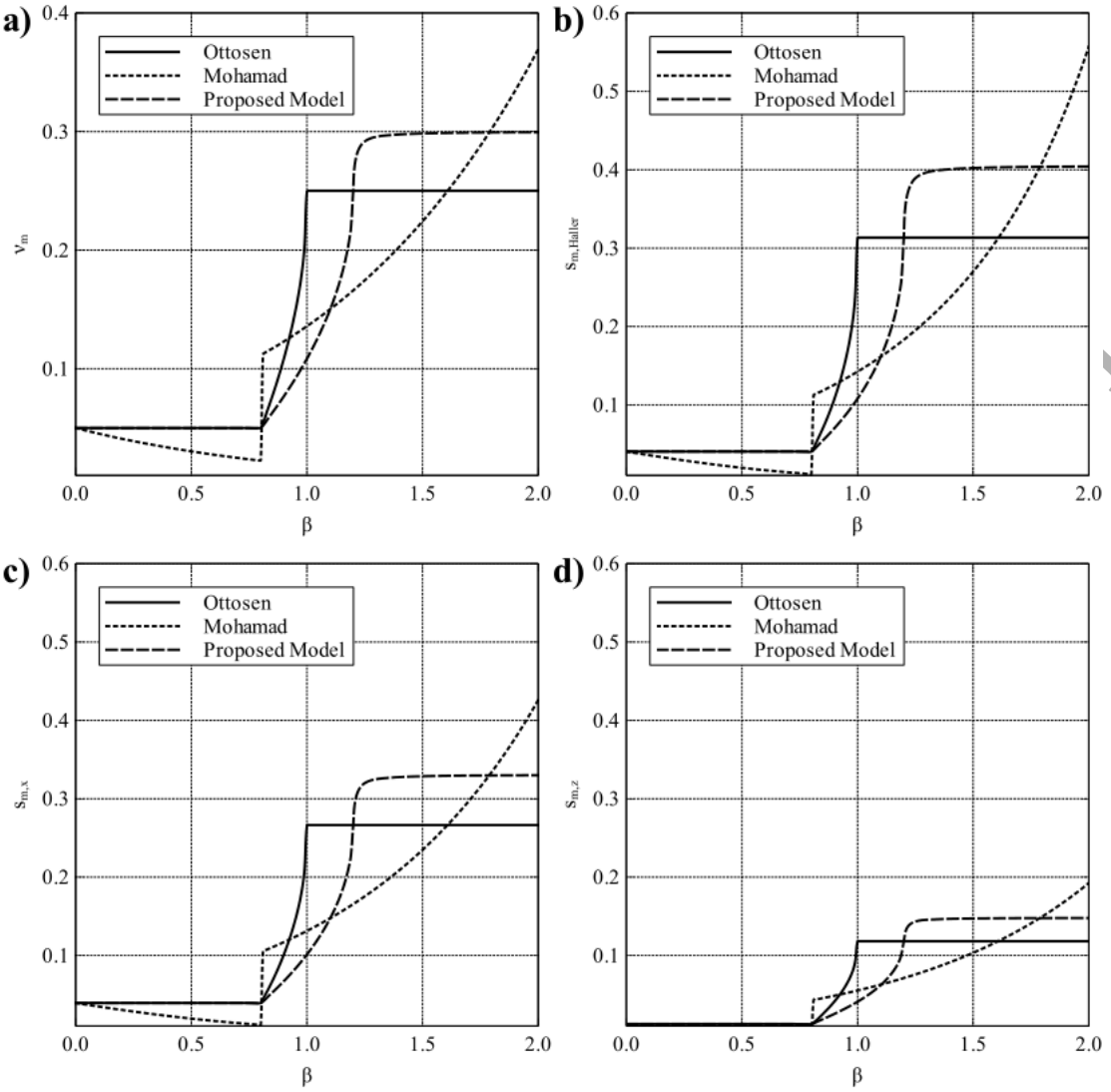

Figure 6 Ottosen, Mohamad and proposed models: (a) the Poisson's ratio of mortar vs. applied stress level, (b) confinement of the mortar joint according to Haller (eq. 17) and (c) & (d) confinement of the mortar joint according to the proposed model in the longitudinal (eq. 15) and transversal (eq. 16) direction respectively.

For the purpose of validating the proposed model, it is compared with the results of a series of three uniaxial compression tests on cylindrical LC mortar samples. The comparison of the model with the experiments is shown in Figure 7. The model is able to capture the behavior of the samples until

failure, employing both the exponential and the hyperbolic branches of the model. Despite the fact that the term "Poisson's ratio" is defined in linear elasticity, the value calculated through the proposed constitutive relation is still referred to using the same term. This is done for the sake of brevity and for distinction between the Poisson's ratio as a material parameter (be it constant, due to Ottosen, Mohamad or the present model) and the apparent Poisson's ratio as calculated from the deformation of the material components. This issue is further explored in section 6.

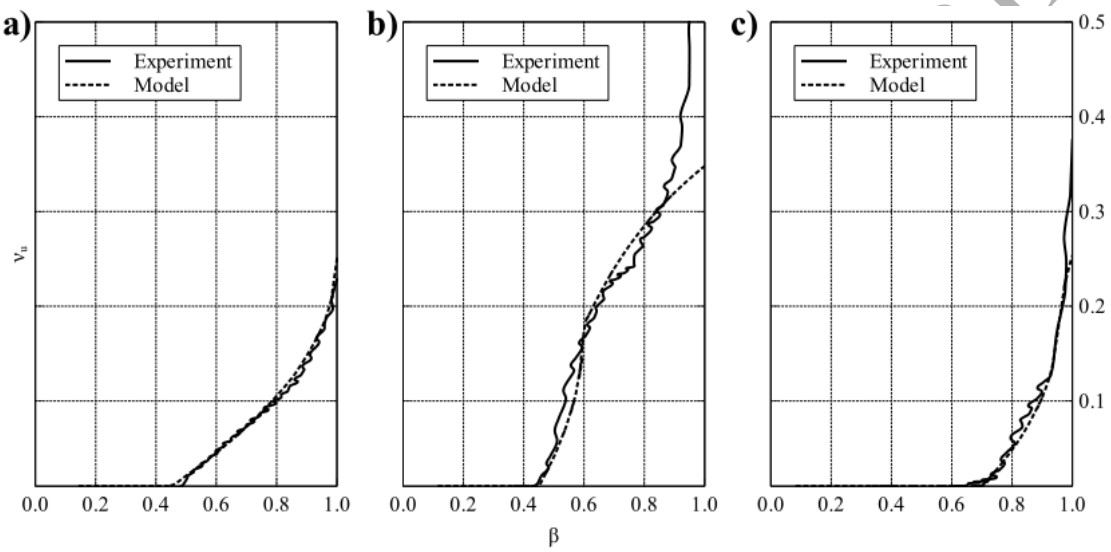

Figure 7 Proposed model for the Poisson's ratio vs. normalized applied stress for hybrid mortar: three tests on the same batch.

The proposed model is further compared to the experimental results from the tests on brick samples. This comparison is shown in Figure 8. While in the present paper the Poisson's ratio of the units was taken as constant, it not being the focus of the research, these results are included in order to demonstrate the suitability of the proposed model for different cases. Despite the very different responses obtained for the two samples, the proposed model can approximate the development of the Poisson's ratio to a satisfactory degree. The exponential increase of the Poisson's ratio measured in the

experiments near the ultimate load should be interpreted as the result of the failure of the sample and not as a material parameter. Therefore, a hyperbolic curve was chosen for the final branch of the proposed model instead of an exponential expression. Further, by manipulation of the parameters of the model, a hyperbolic or exponential increase of the Poisson's ratio may be taken into account. The flexibility of the proposed model consists in its capacity, through manipulation of the numerical parameters, to fully emulate the Ottosen model, in addition to being able to approximate the exponential increase described by the Mohamad model. In nonlinear numerical analysis this behavior of the material is taken into account through softening in compression.

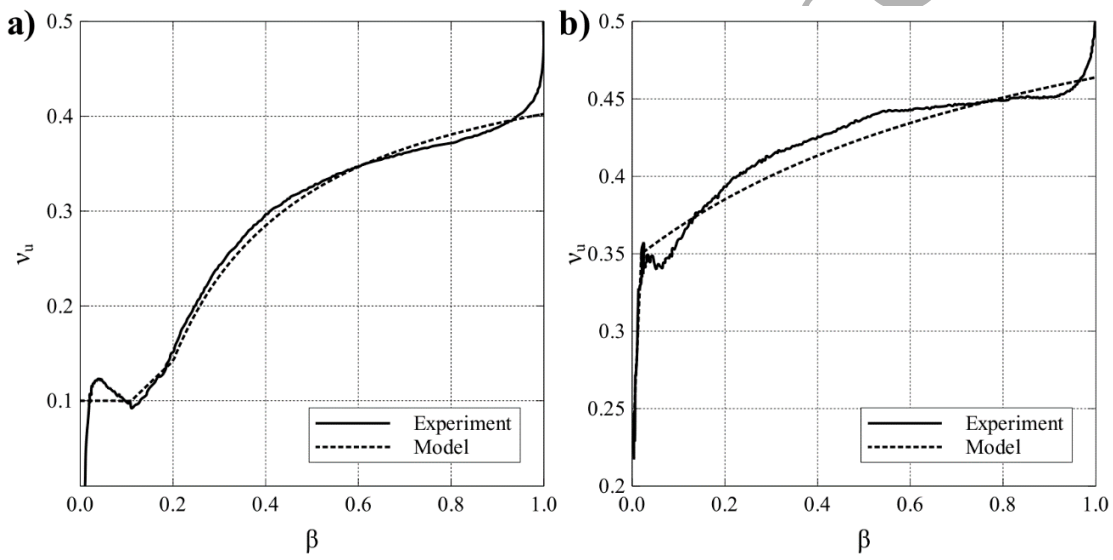

Figure 8 Proposed model for the Poisson's ratio vs. normalized applied stress for brick units: two tests on the same batch.

3.6 Solution of system of equations

The system of equations resulting from the cuboid equations, the integrity variables and the Poisson's ratio is solved iteratively for each load step using a multi-variate Newton-Raphson solution method. The cuboid stress and strain increments are calculated according to the cell total strain

increment and the assumption of trial values for the integrity variables and the Poisson's ratio. Iterations within the load step are performed until the assigned trial values converge with the actual values derived from the stress and strain increment. The iterations, the number of which is indicated with i, are carried out according to

$$\boldsymbol{x}^{i+1} = (1-\omega)\boldsymbol{x}^{i} + \left(\boldsymbol{x}^{i} - J\left(\boldsymbol{x}^{i}\right)^{-1} F\left(\boldsymbol{x}^{i}\right)\right) \tag{33}$$

where $\boldsymbol{x}$ is the vector of variables, F is the vector of equations, J is its Jacobian matrix and ω is the modified Richardson iteration factor. When $\omega = 1$, the iterative method reverts to the standard Newton-Raphson method. When values higher than 1 are assigned, the convergence rate can be increased. Conversely, values between 0 and 1 increase the number of iterations in the load step, but result in more stable convergence. In this study, a value of $\omega = 0.1$ was elected. This resulted in an only small increase of the iterations near the stress-peak and an avoidance of divergence problems.

4. Simulation of masonry compression tests

4.1 Triplets

The comparison between the stress-strain curves obtained from the analyses and the experimental curves is shown in Figure 9. These analyses were carried out using the properties of the batch A mortars and the initial values for the material properties of the bricks without further modification. The obtained peak stress value and initial stiffness of the composite was generally calculated with good accuracy. The inflection of the stiffness during the experiments on the HL triplets was not obtained, however. The post peak behavior, as governed by the softening of the components in compression and tension was also fairly well captured, as in the case of the LP and the LC mortar particularly. The difference in the post-peak curve for the CM triplets indicates that the compressive fracture energy

initially assumed for the mortar is overestimated. However, it is not the main purpose of this paper to engage in parameter calibration for result fitting, especially in the case of the cement mortar.

For the sake of comparison, the results of the same analyses using a constant value for the Poisson's ratio are presented alongside the results using the proposed model. An intermediate value of 0.15 was chosen for the Poisson's ratio for all mortars. In the LP and LC cases the difference between the two approaches is significant. The constant Poisson's ratio assumption cannot account for the confinement of the mortar, leading in turn to an underestimation of the compressive strength. The HL and CM mortar cases, on the other hand, did not present significant differences, their failure mode being dominated by unit cracking and crushing. More details on the initiation and development of damage are presented in Section 6 of this paper.

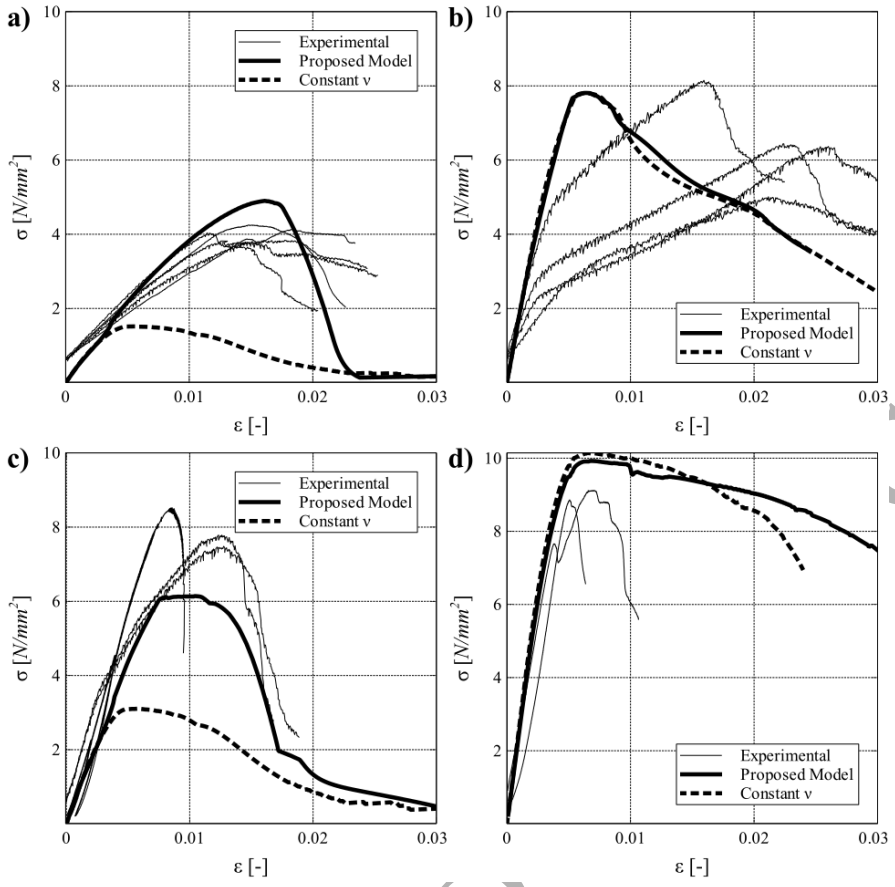

Figure 9 Comparison of experimental and numerical stress strain graphs for masonry triplets: (a) lime putty mortar, (b) natural hydraulic lime mortar, (c) lime-cement mortar and (d) cement mortar triplets.

4.2 Flemish bond wallettes

The analyses of the Flemish bond wallettes were carried out using the parameters for the units and the batch B mortars, for which the Young's modulus was adjusted to match the stiffness of the composite in the experiment. The comparison of the numerical and the experimental results is shown in Figure 10. Overall, good agreement is found between the experimental and numerical results, especially in the case of the LP and CM wallettes, in terms of stiffness and peak stress. In the case of

the LC mortar wallettes the numerically obtained compressive strength is a very good approximation of the average value obtained experimentally. The compressive strength of the HL mortars, however, is underestimated.

The constant Poisson's ratio assumption again results in an underestimation of the compressive strength for the HL, LP and LC cases. The geometrical interlocking of the units in Flemish bond wallettes results in a more complex failure mode compared to the stack bond prism cases. Therefore, underestimating the confinement of the mortar results in a potentially lesser degree of underestimation of the compressive strength of masonry. Nevertheless, the differences between the proposed model and the constant Poisson's ratio assumption are significant in the HL case.

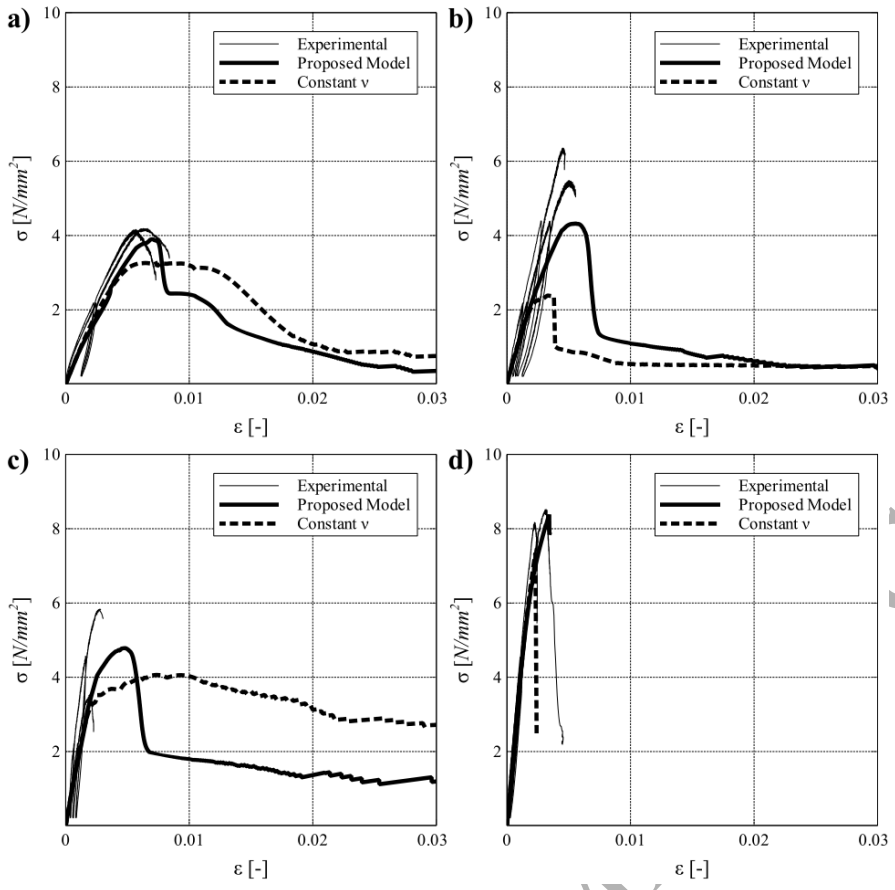

Figure 10 Comparison of experimental and numerical stress strain graphs for masonry wallettes: (a) lime putty mortar, (b) natural hydraulic lime mortar, (c) lime-cement mortar and (d) cement mortar wallettes.

5. Summary of Experimental and Numerical Results For Masonry

The experimental and numerical results for the masonry samples in compression are visually summarized in Figure 11. A logarithmic fit has been presented for the trend of the compressive strength of masonry, illustrating a slight overestimation by the triplet strength for higher values of the compressive strength of the mortar. However, in the case of low strength mortar, where confinement and triaxial effects are decisive, the model performs well both for triplets and wallettes. Comparison of fitted curves, both experimental and numerical, indicate lower compressive strength for wallettes

compared to triplets. The existence of head and collar joints, combined with the staggered arrangement of the units in Flemish bond wallettes results in a decrease of the obtained compressive strength due to differences in dimension ratio, the existence of a larger number of unit mortar interfaces and a different triaxial stress state of the mortar in the bed joints. The difference in compressive strength between triplets and wallettes is more apparent for low strength mortars. The use of high strength cement mortar shifts the failure mode towards compressive yielding of the units, leading to a more uniform obtained strength between typologies, both in the experiments and the numerical analyses.

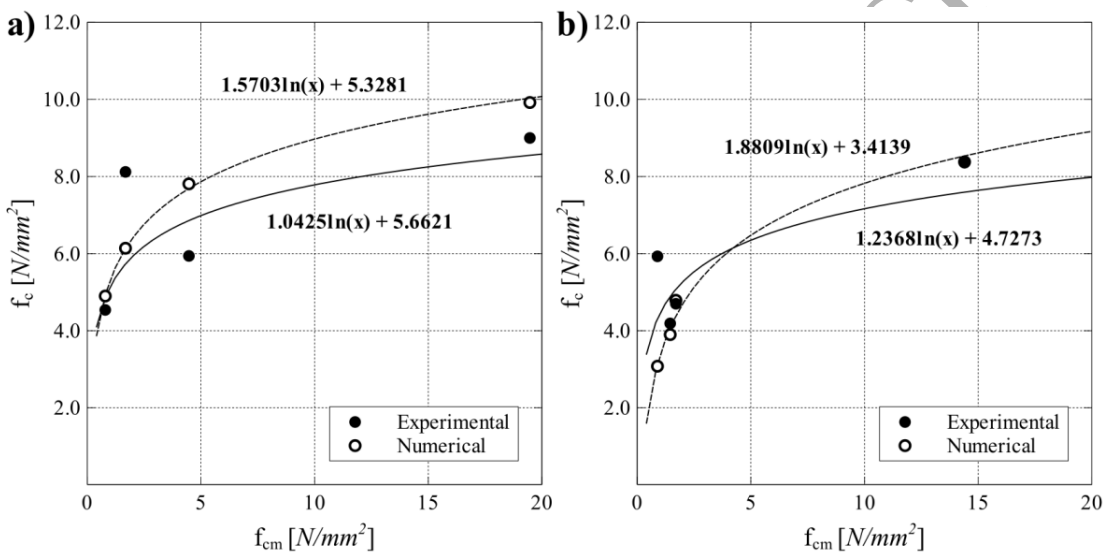

Figure 11 Summary of experimental and numerical results with logarithmic fit (solid line for experiments, dashed lines for numerical results). Compressive strength of mortar vs. compressive strength of masonry for: a) triplets and b) wallettes.

A comparison of the experimentally obtained compressive strength of masonry with closed-form expressions is presented in Table 8. Such expressions have been proposed by researchers [23–27] and others have been adopted for use in analysis and design standards for masonry structures [28]. These models have either an empirical or semi-empirical basis, or account for masonry failure modes in a

simplified way. While closed-form expressions are very easy to employ, they are often characterized by a lack of accuracy when calculations over a wide spectrum of cases is required or when all failure modes are not accounted for.

The CEN model takes into account the compressive strength of both units and masonry. It underestimates the compressive strength of the composite. The Hilsdorf and Francis models give reasonable results for the triplets but overestimate the compressive strength of the wallettes. The Khoo & Hendry model greatly overestimates the compressive strength for the CM cases and, more importantly, does not follow the trend observed for the compressive strength of masonry vs. the compressive strength of mortar. The model by Drougkas et al gives results close to the numerically obtained values and a good estimation of the triplets' strength. The wallette strength was not equally well estimated due to the model being applied without altering the numerical parameters for triaxial confinement. This further illustrates the necessity of experimental determination of the triaxial behavior of mortar prior to its modeling in masonry in compression.

Table 8 Comparison of test results on masonry compressive strength in N/mm^2 with closed form expressions.

		Experiment	Numerical	Hilsdorf [27]	Francis [23]	Khoo & Hendry [26]	Hendry [25]	Drougkas et al [19]	CEN [28]
Triplets	**LP**	4.54	4.90	6.81	7.28	5.03	7.60	4.63	2.56
	HL	5.94	7.81	7.71	7.67	7.25	8.01	7.78	4.31
	LC	8.12	6.14	7.03	7.36	5.81	7.68	7.40	3.21
	CM	9.00	9.92	11.40	9.63	21.63	9.57	9.70	6.70
Wallettes	**LP**	4.19	3.90	6.97	7.34	5.64	7.66	7.37	3.08
	HL	5.93	4.32	6.84	7.45	5.14	7.79	4.36	2.66
	LC	4.70	4.79	7.03	7.81	5.82	8.15	5.98	3.23
	CM	8.36	8.38	10.15	28.76	13.66	13.65	6.29	6.12

6. Parametric Study

6.1 Proposed Model vs. Constant Poisson's Ration

The effect of different approaches for modeling the development of the Poisson's ratio in masonry is investigated through a comparative study, carried out on the LP mortar triplets. Two approaches are here adopted: a constant value of the Poisson's ratio of mortar and a value calculated using the proposed model. A value of 0.25 is assigned to the constant Poisson's ratio, while for the proposed model the values $\nu_{m,1} = 0.05$, $\nu_{m,2} = 0.25$, $\nu_{m,3} = 0.50$, $\beta_1 = 0.5$, $\beta_2 = 2.0$ and $k = 0.5$ are chosen.

The resulting stress-strain curves are shown in Figure 12. The peak-stress using the proposed model is roughly 13% lower and the peak strain is nearly 40% lower, although a stress plateau is formed, extending to roughly 85% of the peak strain obtained with the constant Poisson's ratio. Another feature of the proposed model is the increase in the stiffness of the triplet by 6% at around 30% of the peak load. This stress level coincides with the second inflection point of the proposed model. Overall the two curves are not markedly different in shape, with the exclusion of a small stress plateau obtained for the proposed model. The underlying causes of the response however are made apparent upon examination of the integrity variables.

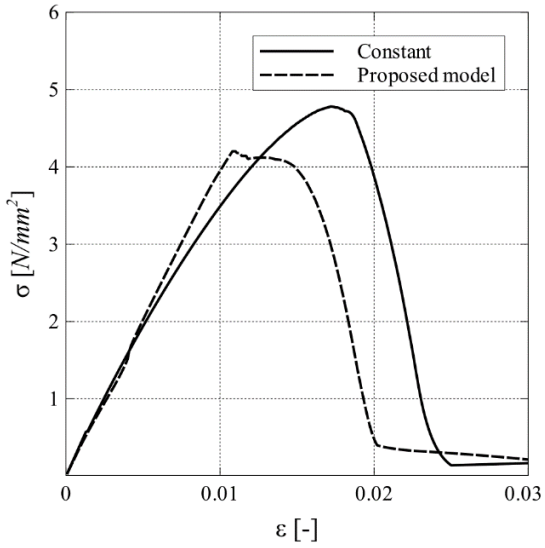

Figure 12 Stress-strain curves for lime-putty mortar triplets using different models for Poisson's ratio of mortar.

The development of the integrity variables of the units and the mortar vs. the applied strain is shown in Figure 13. For the constant Poisson's ratio (Figure 13a) the response is nearly fully determined by the failure of the mortar joint in compression. The compressive damage on the unit is minor and there is no damage registered in tension for either of the components. The obtained damage pattern is markedly different in the case of the proposed model (Figure 13b). The compressive damage in the mortar ceases to increase upon attainment of the peak stress, whereupon a rapid increase in the tensile damage of the unit is registered, coupled with damage in compression. The final softening branch of the response is associated with damage of the mortar joint in tension. Experimental evidence is more in agreement with the failure mode obtained by the adoption of the proposed model, where tensile damage of the unit plays a significant part in the softening behavior of the masonry.

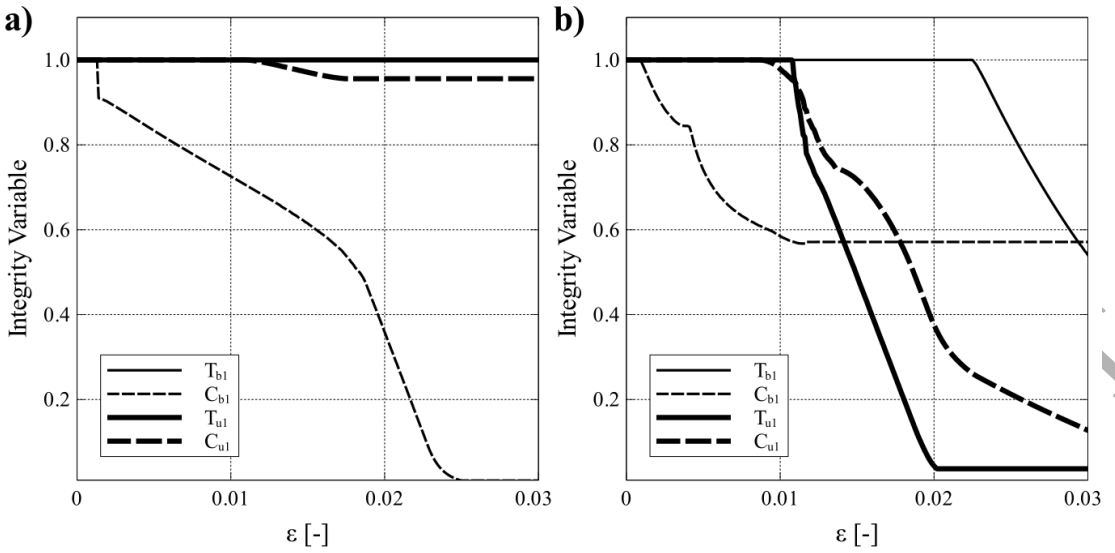

Figure 13 Development of integrity variables for (a) a constant Poisson's ratio and (b) adopting the proposed model.

Figure 14 illustrates the development of the Poisson's ratio ν_m as an assigned material property (constant or from eq. 32) for the mortar as well as in terms of apparent deformation on the two components and in both lateral directions, vs the applied vertical strain. These apparent Poisson's ratios $\nu_{iy,n}$ of any component n are calculated by the expression:

$$\nu_{iy,n} = -\frac{\varepsilon_{ii,n}}{\varepsilon_{yy,n}} \tag{34}$$

where i is the direction under consideration (horizontal x or transversal z) and $\varepsilon_{yy,n}$ is the vertical strain applied on the component in the load step.

In the case of the constant model, the components maintain a constant apparent Poisson's ratio, although different from the value assigned as a material property. The mortar in the longitudinal direction remains practically undeformed, whereas in the transversal direction its apparent Poisson's ratio is lower than the assigned material value. This is to be expected given the confinement effect.

The unit exhibits an apparent Poisson's ratio higher than the assigned material value, the difference being higher in the longitudinal direction. Adopting the proposed model, the response changes radically (see Figure 14b). The mortar again remains largely undeformed longitudinally until the peak stress, whereupon its apparent Poisson's ratio increases rapidly. A similar response is registered in the transversal direction, with the increase in the apparent Poisson's ratio being more marked, in fact increasing to values 60% higher than the maximum value assigned as a material property. Both apparent ratios settle at values near the assigned material value for the given level of stress. The shift in the apparent Poisson's ratio of the unit is more modest, with the increase being higher in the longitudinal direction.

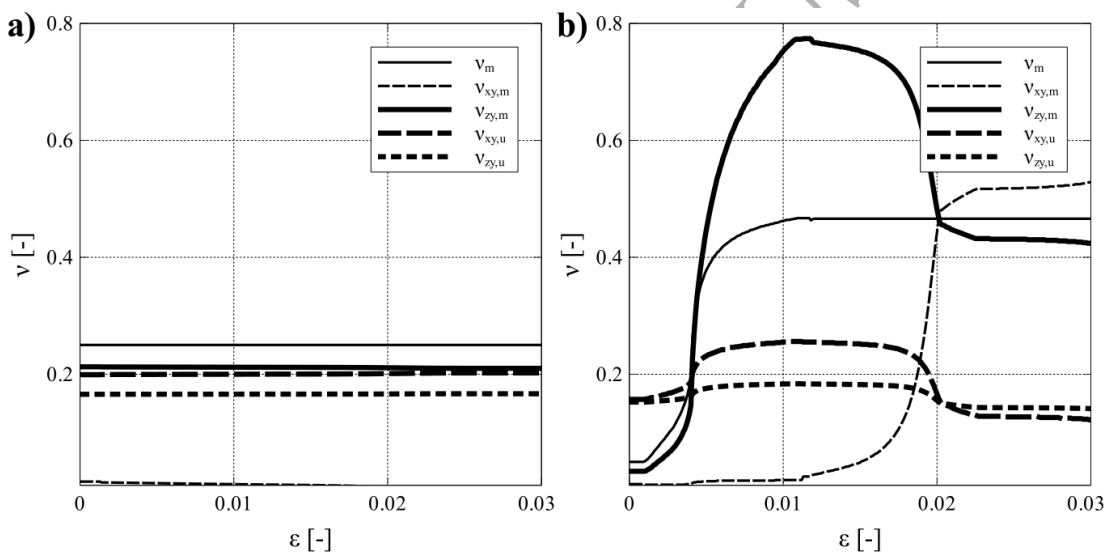

Figure 14 Development of calculated (eq. 32) and apparent Poisson's ratio of components vs. the applied vertical strain for (a) a constant Poisson's ratio of mortar and (b) adopting the proposed model.

Figure 15 illustrates the apparent secant Young's modulus of the masonry composites and components vs the applied strain. For a constant Poisson's ratio, the confinement appears to be initially

overestimated, as evidenced by the normalized apparent Young's modulus of the mortar being higher than 1. Subsequently, the response of the masonry is shown to be entirely influenced by the crushing of the mortar joint in compression. For the proposed model of the Poisson's ratio the confinement is initially low, leading to a reduction of the apparent Young's modulus of the mortar early in the response. After an increase in the Poisson's ratio for a higher applied load, the confinement of the joint is activated, leading to an increase of the stiffness. Following that, the secant Young's modulus of all components steadily declines until the peak force is applied, after which the secant stiffness of both components tends towards zero.

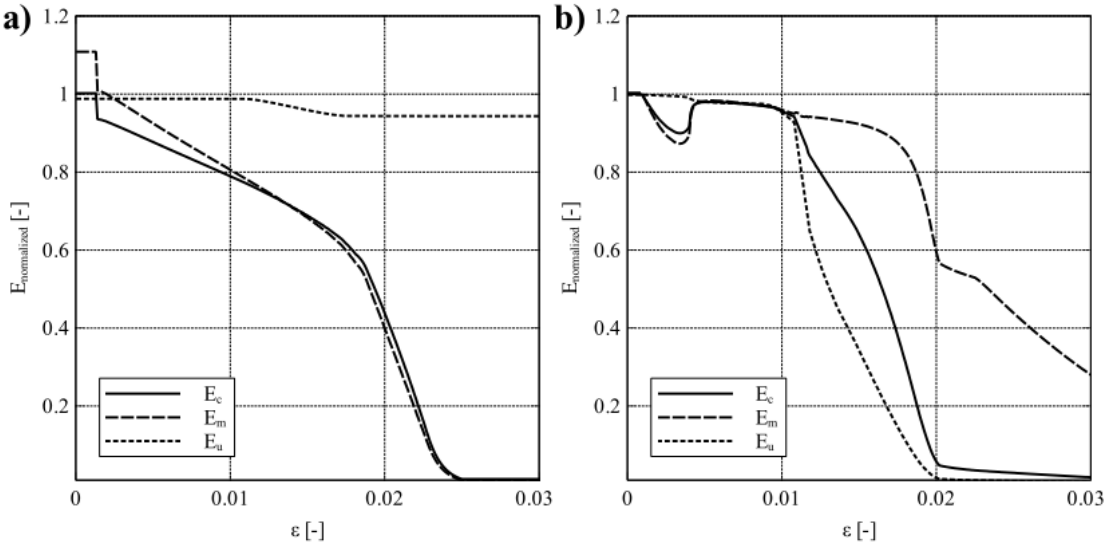

Figure 15 Development of apparent secant Young's modulus for masonry composite and components, normalized over initial material values: (a) for constant value of Poisson's ratio and (b) for adoption of proposed model.

The results from the constant value of the Poisson's ratio of mortar indicate that in order to obtain an accurate stress-strain curve it is necessary to assume a high value for this parameter. An even higher value is required for the activation of the failure mode in tension for the units, unless a particularly low

value for the tensile strength is assumed. Both of these measures, particularly the former, are not in agreement with experimentally observed behavior of masonry materials and have a strong influence on efforts focusing on the numerical simulation of masonry in compression.

The major differences in assigned and apparent Poisson's ratios for both masonry components here investigated shed light on differences observed between their behavior in standalone tests and as observed in masonry composites under mechanical loading, as for example by optical methods such as Digital Image Correlation [2]. These differences are noted even at the central area of the linear branch in the response of the masonry composite. While it appears that deformations parallel to the load may be accurately measured, the secant modulus being nearly constant for the components at that range, lateral deformations may fluctuate significantly as the Poisson's ratio of the mortar shifts under increasing load.

6.2 Proposed Model Parameters

The sensitivity of the response to the parameters of the proposed Poisson's ratio is illustrated in Figure 16. Reverting to a constant value approach, the compressive strength of the LP triplets increases for an increase of the Poisson's ratio, up to the point when its confinement leads to high tensile stresses in the unit. The ductility can increase substantially when the compressive strength of masonry is lower (Figure 16a). The k parameter of the model, controlling the shape of the hyperbolic curve, can increase the excessive tensile stresses in the unit when low, or conversely decrease them when high (Figure 16b). This is due to the lower rate of increase of the Poisson's ratio in the constitutive relation in the latter case. When only the exponential or only the hyperbolic branch of the model are employed (Figure 16c) not only the strength, but also the stiffness of the composite is affected. A noticeable increase of the initial stiffness is registered when considering only the hyperbolic branch due to the higher slope of the constitutive curve for $k = 0.5$. Finally, the response is also sensitive to the position

of the first inflection point of the curve as controlled by β_1. A higher value for β_1 leads to a delayed reaching of the exponential branch of the constitutive model. This results in an initial decrease of the apparent stiffness of the masonry followed by a further increase. This is not unlike the change of stiffness noted for the HL triplets (Figure 9b).

Overall, it becomes apparent that in a computational context the prediction of the compressive strength of masonry is very sensitive to the triaxial confinement afforded on the mortar joint, which is in turn very sensitive to the calculated and apparent Poisson's ratio. It is therefore critical that both aspects of masonry mortars be experimentally investigated jointly. This is a necessary step before the adoption of theoretically robust, rather than semi-empirical, approaches to the development of the Poisson's ratio under increasing stress, the inclusions of mortar damage in the models and the complete evaluation of the behavior of mortar in masonry under compression.

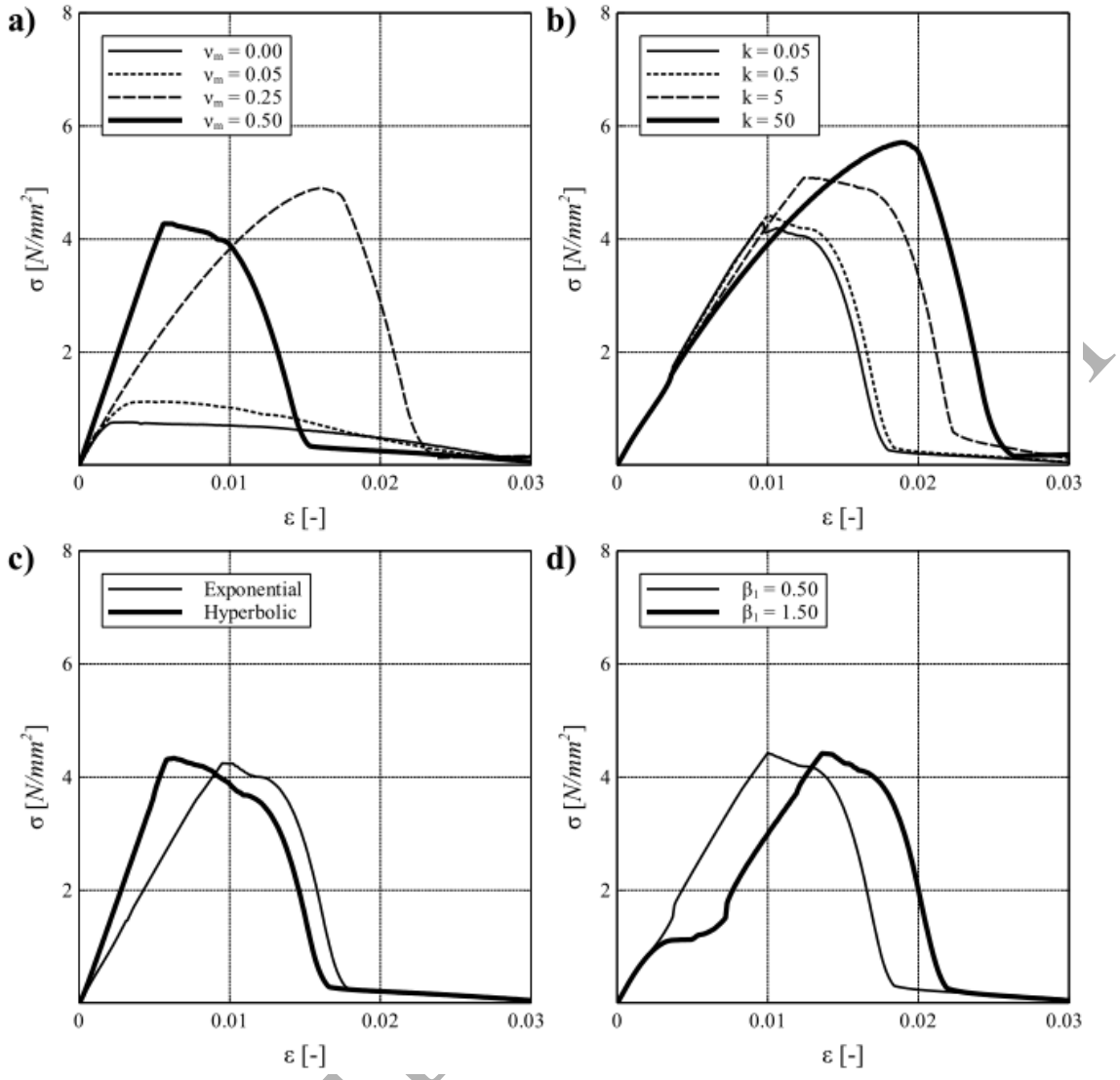

Figure 16 Sensitivity of the compressive behavior of masonry to Poisson's ratio of mortar parameters: a) constant values of Poisson's ratio, b) hyperbolic curve shape of proposed model, c) hyperbolic or exponential shape of model, and d) location of first inflection point.

7. Conclusions

A model for the micro-mechanical analysis of masonry structures subjected to mechanical loading has been improved and expanded to include shifting values for the Poisson's ratio of mortar under increasing vertical load. The model is capable of depicting the compressive and tensile damage on

masonry components in members subjected to mechanical loading. The development of stress, deformation and material degradation is achieved with minimal computational cost and good accuracy.

Further, a model for the increase of the Poisson's ratio of mortar is proposed. Incorporated into the micro-mechanical model, it highlights the inadequacy of a constant Poisson's ratio for mortar in a computational framework for the accurate micro-modeling of masonry.

The model allows the detailed study of the behavior of mortar confined in masonry joints. The lateral expansion of the mortar in the joint emerges as the principal phenomenon determining the behavior of masonry in compression. This effect is quantified according to material and geometric parameters. Taking into account the variation of the Poisson's ratio in the mortar for increasing vertical stress, the apparent Poisson's ratio in all components changes radically during loading.

In a computational context, the development of damage in the components of the masonry changes significantly when the variation of the Poisson's ratio of the mortar is taken into account. The resulting failure mode is consistent with experimentally observed failure, where compressive and tensile damage extends to both mortar and units. Therefore, the Poisson's ratio of mortar in masonry under compression emerges as a parameter that cannot be determined as an elasticity theory parameter in a straightforward manner.

Suggestions for future work include a similar study for the behavior of solid clay bricks under increasing vertical loading, especially in regards to the development of their Poisson's ratio. Evidence has been provided that the Poisson's ratio of bricks is not constant, a fact which might prove critical in combination with cement mortars sufficiently stiff to provide confinement to the units when the composite is subjected to vertical compressive stress. Similarly, the study of the development of the

Poisson's ratio in mortar under different levels of confinement arises as an important subject, for which special experimental setups need to be developed.

Acknowledgements

Funding for this work was procured through the GEPATAR project ("GEotechnical and Patrimonial Archives Toolbox for ARchitectural conservation in Belgium" BR/132/A6/GEPATAR), which is financially supported by BRAIN-be, Belspo.

References

[1] Pelà L, Cervera M, Roca P. An orthotropic damage model for the analysis of masonry structures. Constr Build Mater 2013;41:957–67. doi:10.1016/j.conbuildmat.2012.07.014.

[2] Bejarano-Urrego L-E, Verstrynge E, Giardina G, Van Balen K. Crack growth in masonry: Numerical analysis and sensitivity study for discrete and smeared crack modelling. Eng Struct 2018;165:471–85. doi:10.1016/j.engstruct.2018.03.030.

[3] Adam JM, Brencich A, Hughes TG, Jefferson T. Micromodelling of eccentrically loaded brickwork: Study of masonry wallettes. Eng Struct 2010;32:1244–51. doi:10.1016/j.engstruct.2009.12.050.

[4] Brencich A, Gambarotta L. Mechanical response of solid clay brickwork under eccentric loading. Part I: Unreinforced masonry. Mater Struct 2005;38:257–66. doi:10.1617/14134.

[5] Drougkas A, Roca P, Molins C. Numerical prediction of the behavior, strength and elasticity of masonry in compression. Eng Struct 2015;90:15–28. doi:10.1016/j.engstruct.2015.02.011.

[6] Lourenço P, Pina-Henriques JL. Validation of analytical and continuum numerical methods for estimating the compressive strength of masonry. Comput Struct 2006;84:1977–89.

doi:10.1016/j.compstruc.2006.08.009.

[7] Haller P. Hochhausbau in Backstein: die technischen Eigenschaften von Backstein-Mauerwerk für Hochhäuser. Schweizerische Bauzeitung 1958;76:411–9.

[8] Zucchini A, Lourenço P. Mechanics of masonry in compression: Results from a homogenisation approach. Comput Struct 2007;85:193–204. doi:10.1016/j.compstruc.2006.08.054.

[9] Drougkas A, Roca P, Molins C. Analytical Micro-Modeling of Masonry Periodic Unit Cells – Elastic Properties. Int J Solids Struct 2015;69–70:169–88. doi:10.1016/j.ijsolstr.2015.04.039.

[10] Pande GN, Kralj B, Middleton J. Analysis of the compressive strength of masonry given by the equation fk = K fb^ α fm^β. Struct Eng 1994;71:7–13.

[11] Verstrynge E, Schueremans L, Van Gemert D. Time-dependent mechanical behavior of lime-mortar masonry. Mater Struct 2011;44:29–42. doi:10.1617/s11527-010-9606-8.

[12] Barbosa CS, Lourenço P, Hanai JB. On the compressive strength prediction for concrete masonry prisms. Mater Struct 2010;43:331–44. doi:10.1617/s11527-009-9492-0.

[13] Hayen R, Van Balen K, Van Gemert D. Triaxial interaction of natural stone, brick and mortar in masonry constructions. Build Mater Build Technol to Preserv Built Heritage, WTA Schriftenr 2009:333–52.

[14] Drougkas A, Roca P, Molins C. Compressive strength and elasticity of pure lime mortar masonry. Mater Struct 2016;49:983–99. doi:10.1617/s11527-015-0553-2.

[15] Mohamad G, Lourenço P, Roman HR. Mechanics of hollow concrete block masonry prisms under compression: Review and prospects. Cem Concr Compos 2007;29:181–92.

doi:10.1016/j.cemconcomp.2006.11.003.

[16] Federátion Internationale du Béton. The fib Model Code for Concrete Structures 2010. Wiley and Sons; 2013.

[17] CEN. EN 1015-11 - Methods of test for mortar for masonry - Part 11: Determination of flexural and compressive strength of hardened mortar. 2007.

[18] Aboudi J, Pindera M-J. Micromechanics of metal matrix composites using the Generalized Method of Cells model (GMC) - User's guide. NASA; 1992.

[19] Drougkas A, Roca P, Molins C. Nonlinear Micro-Mechanical Analysis of Masonry Periodic Unit Cells. Int J Solids Struct 2016;80:193–211.

[20] Feenstra PH, Borst R De. A composite plasticity model for concrete. Int J Solids Struct 1996;33:707–30.

[21] Hsieh SS, Ting EC, Chen WF. A plastic-fracture model for concrete. Int J Solids Struct 1982;18:181–97.

[22] Ottosen NS. Constitutive Model for Short-Time Loading of Concrete. J Eng Mech Div 1979;105:127–41.

[23] Francis A, Horman C, Jerrems L. The effect of joint thickness and other factors on the compressive strength of brickwork. Proc. 2nd Int. Brick Block Mason. Conf., 1971, p. 31–7.

[24] Drougkas A, Roca P, Molins C, Alegre V. Compressive Testing of an Early 20th Century Brick Masonry Pillar. Mater Struct 2016;49:2367–81. doi:10.1617/s11527-015-0654-y.

[25] Hendry AW. Structural masonry. Macmillan Education Limited; 1990.

[26] Khoo CL, Hendry AW. Strength tests on brick and mortar under complex stresses for the development of a failure criterion for brickwork in compression. Proc Br Ceram Soc 1973;21:57–66.

[27] Hilsdorf HK. Investigation into the failure mechanism of brick masonry loaded in axial compression. In: Johnson FB, editor. Des. Eng. Constr. with Mason. Prod., Houston Tex.: 1969, p. 34–41.

[28] CEN. EN 1996-1-1 - Eurocode 6: Rules for reinforced and unreinforced masonry. 2005.

[29] ACI. ACI 530.1-11. Building Code Requirements and Specification for Masonry Structures and Related Commentaries. 2011.